BEAM POSITION MONITORS FOR CIRCULAR ACCELERATORS

Shigenori Hiramatsu

KEK, 1-1 Oho, Tsukuba, Ibaraki, 305-0801, Japan

Abstract

Beam position monitor (BPM) systems are one of the most important system for tuning up accelerators to accelerate charged particle beams in a good condition. BPMs measure the betatron orbit or the closed orbit of the circulating beam in the accelerator, and beam optics parameters $\beta(s)$, betatron phase advance $\phi(s)$, etc. can be evaluated from the BPM data. For tuning up accelerators, it is required that BPMs can measure beam orbits accurately. To realize BPM system with good accuracy, we have to concern many issues related to the BPM system.

BEAM INDUCED CHARGE DISTRIBUTION ON BEAM CHAMBERS

Electrostatic type BPM pickups detect the beam induced charge imbalance among pickup electrodes. To investigate induced charge on pickup electrodes, it is helpful to investigate the beam induced charge distribution on the beam chamber surface. For the case of the beam chamber with circular cross section, the pencil beam located at

$$(x, y) = (r\cos\theta, r\sin\theta)$$

induces the surface charge density distribution on the chamber surface expressed as

$$\sigma(R, \phi) = -\frac{\lambda}{2\pi R} \cdot \frac{R^2 - r^2}{R^2 + r^2 - 2rR\cos(\phi - \theta)}$$

$$= -\frac{\lambda}{2\pi R}\left\{ 1 + 2\sum_{n=1}^{\infty}\left(\frac{r}{R}\right)^n \cos n(\phi - \theta)\right\}, \quad (1)$$

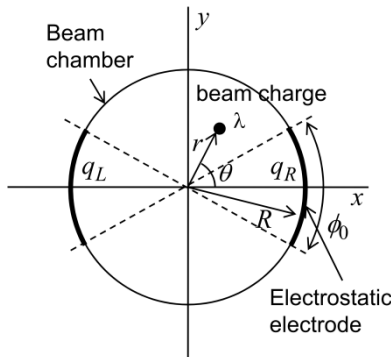where λ is the line charge density of the beam, R is the radius of the chamber, and ϕ is the azimuth.

Figure 1: Cross section of BPM pickup model.

When two pickup electrodes with angular width ϕ_0 are placed at 0° and 180° as shown in Fig. 1, the induced charge on the electrodes q_R and q_L are given by integration of Eq. (1) in the region of $(-\phi_0/2, \phi_0/2)$ and

$(\pi-\phi_0/2, \pi+\phi_0/2)$ for ϕ. The response of the difference q_R-q_L normalized by the sum q_R+q_L for the beam position x is shown in Fig. 2. The difference-over- sum ratio (Δ/Σ) of the induced charge on two electrodes is proportional to the beam position displacement in x-direction from the chamber center [1] in the vicinity of the camber center ($r<<R$),

$$\frac{q_R - q_L}{q_R + q_L} = \kappa x, \quad (2)$$

where the sensitivity factor κ is given by

$$\kappa = \frac{2\sin(\phi_0/2)}{R\phi_0/2}. \quad (3)$$

Figure 2 shows dependence of Δ/Σ on the beam position x for y=0. It is noted that the dependence of $\log(q_R/q_L)$ is more linear than that of Δ/Σ.
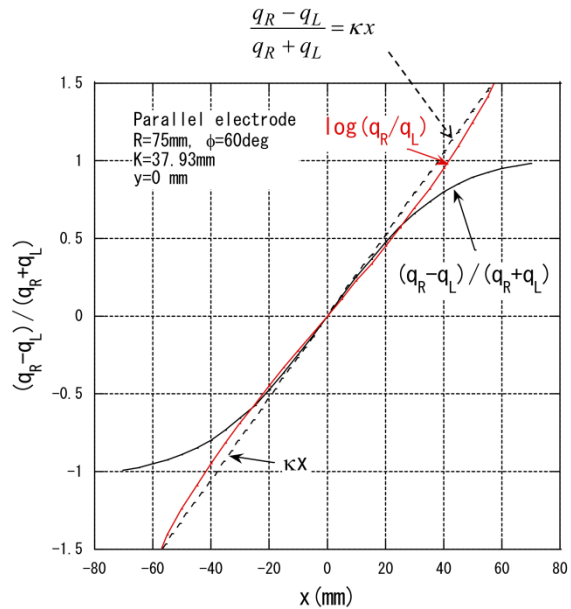

Figure 2: Response of Δ/Σ of the induced charge on the electrodes for the beam position x with the assumption of y=0.

Finite Boundary Element Methods

For the arbitrary shape of the chamber cross section, the beam induced charge can be calculated using the finite boundary element method [2]. The two dimensional potential $\phi(r)$ in the beam chamber is given by

$$\phi(\mathbf{r}) = \oint_{\text{surface}} \ln\left(\frac{1}{|\mathbf{r} - \mathbf{r}'(s)|}\right)\sigma(s)ds + \lambda\ln\left(\frac{1}{|\mathbf{r} - \mathbf{r}_0|}\right). \quad (4)$$

In the right hand side, the 1st term and 2nd term are the potential caused by the induced charge density $\sigma(s)$ on the chamber surface and the beam charge λ, respectively.

Supposing $\phi(\boldsymbol{r})=0$ at the chamber surface, Eq. (4) becomes the integral equation for $\sigma(s)$

$$\oint_{\text{surface}} \ln\left(\frac{1}{|\boldsymbol{r}-\boldsymbol{r}'(s)|}\right)\sigma(s)ds = -\lambda\ln\left(\frac{1}{|\boldsymbol{r}-\boldsymbol{r}_0|}\right). \quad (5)$$

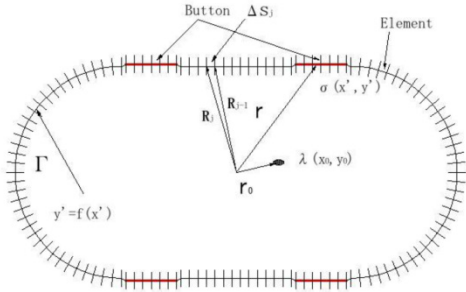This equation can be solved numerically by dividing the chamber surface in many fine elements as show in Fig. 3.

Figure 3: Meshes of the finite boundary element method.

Triangle Cut Rectangular Pickup

As an example of the calculation by finite boundary element method, the beam induced charge distribution on the rectangular chamber (Fig. 4) is shown in Fig. 5. Integrating the induced charge on the electrodes, we obtain the induced charge on the pair of triangle cut rectangular electrodes shown in Fig. 6. The Δ/Σ ratio of the induced charge on two electrodes is shown in Fig. 7. As shown in the figure, the Δ/Σ depends on only one direction of the beam position displacement (in this example, it depends only on x). This type of the pickup electrode is widely used in various accelerators because of its linear response for the beam position displacement.
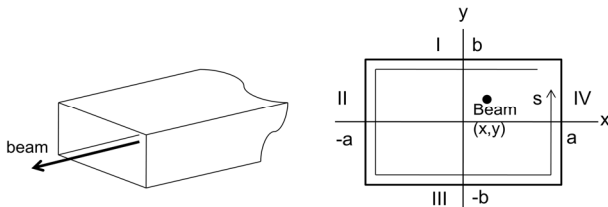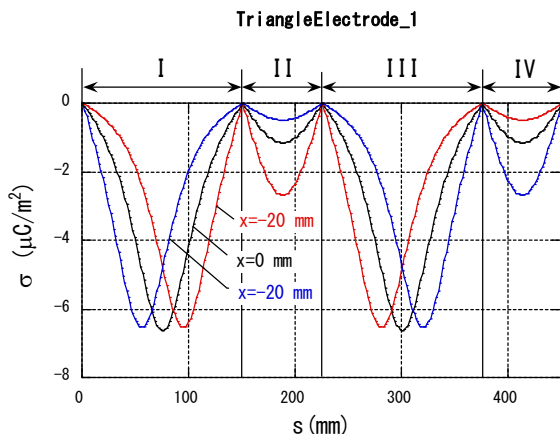

Figure 4: Rectangular beam chamber.

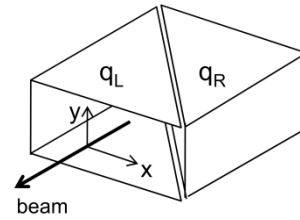Figure 5: Beam induced charge density distribution on the inner surface of the rectangular beam chamber.

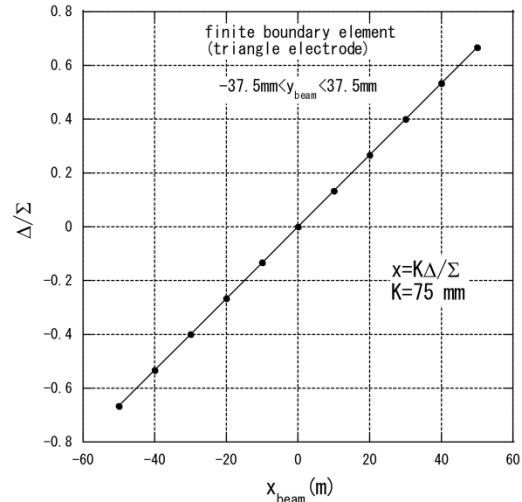Figure 6: Triangle cut rectangular electrode.

Figure 7: Δ/Σ as a function of x.

Parallel Plate Pickup Electrodes

In practice the potential of the pickup electrode is not zero. The electric field in the BPM is affected by the electrode potential (signal voltage) and the induced charge on the electrode changes from the case of $\phi=0$. We consider the BPM pickup as shown in Fig. 8 where the external capacitor C and the resistor R are connected between the electrode and the beam chamber. Usually the condition of $CR \gg \tau_b$ (beam-bunch-length in time) is satisfied to reproduce the bunch shape in the observed signal.
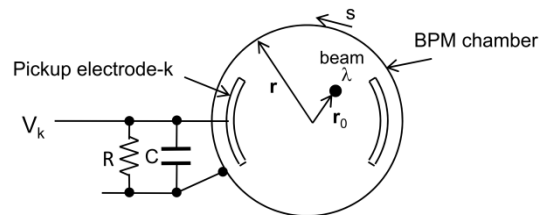

Figure 8: Loaded electrode by C and R.

Under this condition the induced charge distribution $\sigma(s)$ and the electrode potential V_k are given by

$$\left.\begin{array}{l}\oint_{\substack{chamber \\ +electrodes}} \ln\left(\frac{1}{|\boldsymbol{r}-\boldsymbol{r}'(s)|}\right)\sigma(s)ds + \lambda\ln\left(\frac{1}{|\boldsymbol{r}-\boldsymbol{r}_0|}\right) \\[2em] = \begin{cases} 0 & (\boldsymbol{r}\text{ is on the chamber surface}) \\ 2\pi\varepsilon_0 V_k & (\boldsymbol{r}\text{ is on the electrode - k surface}) \end{cases} \\[2em] \oint_{electrode\text{-}k}\sigma(s)ds = -\dfrac{V_k}{C} \end{array}\right\}.$$

The numerical solution of $\sigma(s)$ and V_k are obtained by solving above equations using the finite boundary element method as similar to the previous example.
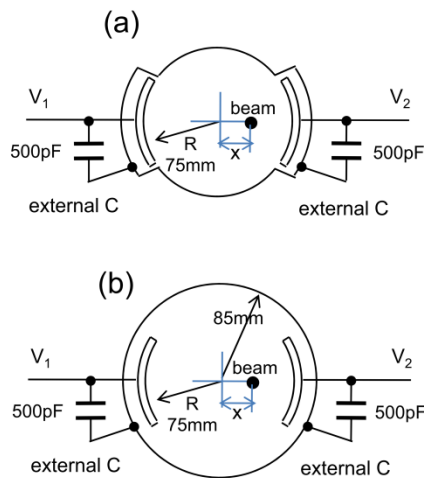

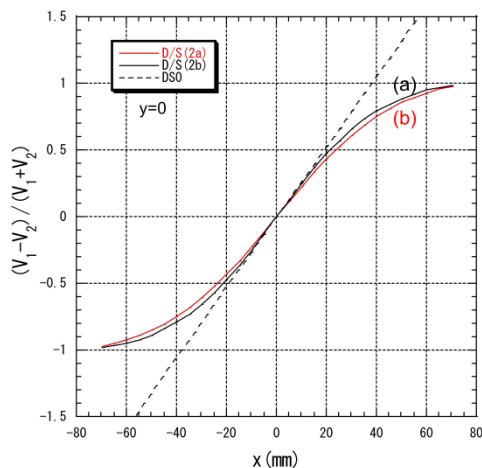Figure 9: Two examples of BPM structure.

Figure 10: Δ/Σ responses of BPMs shown in Fig. 9. Dashed line indicates κx with κ given by Eq. (3).

In the case of Fig. 9(a) where the front surfaces of electrodes coincide to the beam chamber surface, the calculated sensitivity κ of Δ/Σ of the induced charge on the electrodes is equal to the Δ/Σ of Fig. 2. However, if we have a gap between the electrode surface and the chamber surface as shown in Fig. 9(b), κ becomes to be

smaller than that of the case (a) because the electric field outside of the electrode concentrates to the electrode edge so that the effective angle width of the electrode becomes wider than that given by Eq. (3). The difference of κ between the case (a) and the case (b) is about 10% as shown in Fig. 10 for dimensions shown in Fig. 9. This situation means that the sensitivity of the BPM pickup depends on the surroundings of the pickup electrodes even though the same electrode structure is employed and we need to calibrate the response of Δ/Σ at the calibration stand using the stretched wire method etc.

Diagonal Cut Cylinder

Besides the triangle cut rectangular electrode, the diagonal cut cylinder electrode as shown in Fig. 11 is also used widely because of its linear response for the beam position displacement. The beam induced charge on each electrode is given by the integration of Eq. (1) on the electrode:

$$q_\pm(x,y) = \int_0^{2\pi} a\tan\theta(1\pm\cos\phi)\sigma(a,\phi;x,y)d\phi$$

$$= -\lambda\frac{L}{2}\left(1\pm\frac{x}{a}\right). \tag{6}$$

Therefore we have completely linear response of the Δ/Σ ratio for the beam position x:

$$\frac{q_+-q_-}{q_++q_-} = \frac{x}{a}.$$

This type of BPM pickup is used in the J-Parc proton synchrotron [3] because of the excellent linear response to detect the center position of the large size beam accurately.
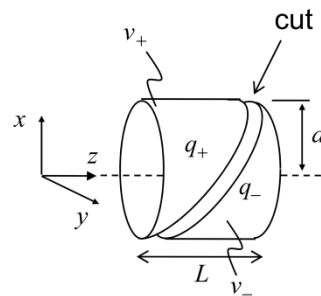

Figure 11: Diagonal cut cylinder.

Coupling between Electrodes

Since a BPM pickup consists of a pair of pickup electrodes, the output of a pickup electrode is affected by the capacitive coupling with another electrode depicted as in Fig. 12.
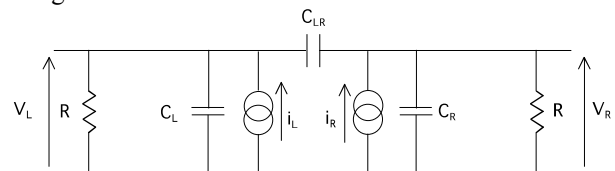

Figure 12: Capacitive coupling between pickup electrodes.

The coupling capacitances between electrodes were measured for the prototype BPM of the J-Parc MR with diagonal cut electrodes as shown in Fig. 13 and the coupling effect was evaluated [3]. The measured electrode capacitances of a horizontal pair C_L and C_R are about 200 pF, and the coupling capacitance C_{RL} is 7.5pF. The estimated sensitivity factor κ from the measured capacitances reproduces well the measured κ shown in Fig. 14. The degradation of κ by the coupling capacitance is not negligible small for >5 MHz. At the BPM system of the J-Parc MR, the coupling effect can be neglected because the frequency component around 2 MHz of the pickup signal is detected.
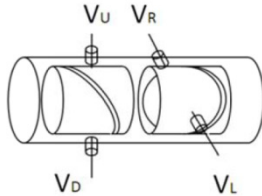

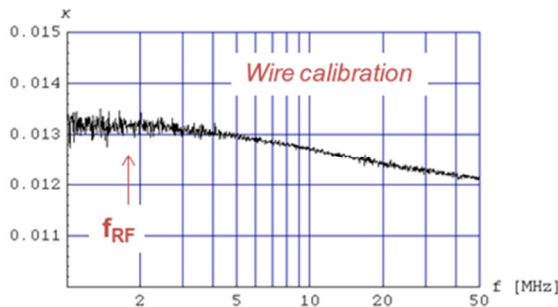Figure 13: BPM pickup with diagonal cut electrodes at J-Parc.

Figure 14: Measured sensitivity factor κ as a function of frequemcy.

Four Button Electrodes BPMt

The BPM pickup for the electron accelerators with short bunch length consists of small electrostatic pick up electrodes called as button electrodes as shown in Fig. 15 [4].
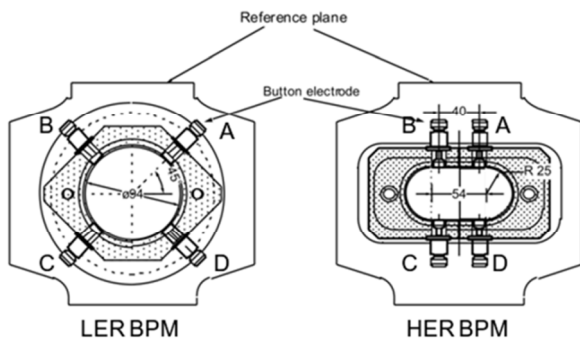

Figure 15: BPM pickups of KEKB.

The distribution of the beam induced charge can be calculated by finite boundary element method. Figure 16 shows an example of the mesh of the boundary for the calculation.
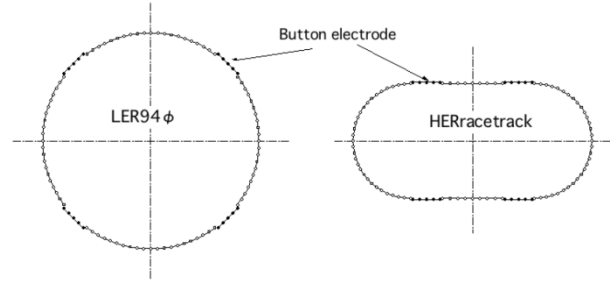

Figure 16: Mesh of the boundary element method.

The calculated charge distribution is shown in Fig. 17 for the beam located at the chamber center. The red points show the surface charge density on the button electrode surface and blue points show the charge distribution on the chamber surface.
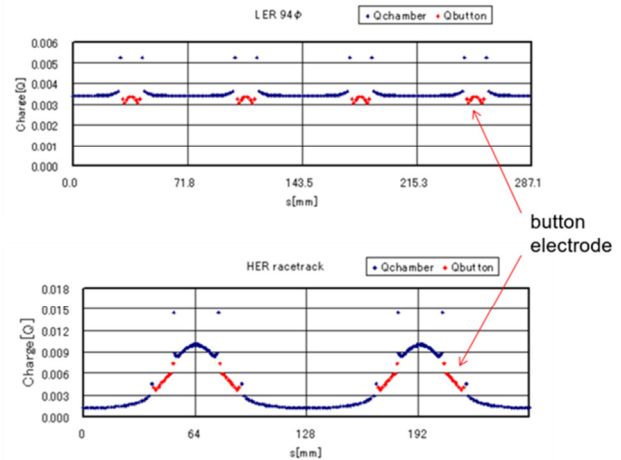

Figure 17: The beam induced charge distribution in BPM pickup shown in Fig. 15.

The beam position (x, y) is determined from the Δ/Σ ratio defined as

$$X = \frac{A + D - B - C}{A + B + C + D}, \quad Y = \frac{A + B - C - D}{A + B + C + D},$$

where A, B, C and D are the outputs of the buttons shown in Fig. 15. We call the correspondence between (X, Y) and (x, y) as mapping:

$$\left. \begin{array}{l} x = F_x(X, Y) \\ y = F_y(X, Y) \end{array} \right\}.$$

The mapping functions $F_x(X,Y)$ and $F_y(X,Y)$ are determined from the measurement at calibration stand or the calculation based on the finite boundary element method. The measured X and Y at the calibration stand are shown in Fig. 18 where each point represents (X, Y) for calibration antenna position or the beam position (x, y) which is changed step-by-step.
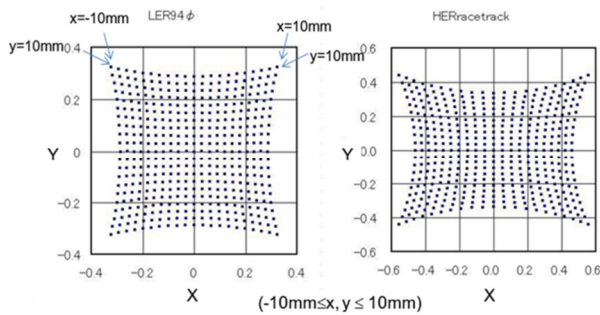
Figure 18: Mapping of the BPM.

SIGNAL PROCESSING

Pickup Response

The equivalent circuit of the electrostatic pickup electrode is shown in Fig. 19 and the signal response is expressed by

$$V(\omega) = \frac{j\omega CR}{1 + j\omega CR} \frac{Q(\omega)}{C},$$

where Q is the beam induced charge on the electrode. This response is equivalent to the response of a high-pass filter with the low frequency cut-off of $1/CR$. To reproduce the bunch shape in the observed signal V, the condition of $CR >> \tau_b$ (bunch length in time) is required. The signal voltage is proportional to $1/C$ so that the estimation of C is required to estimate the signal magnitude.
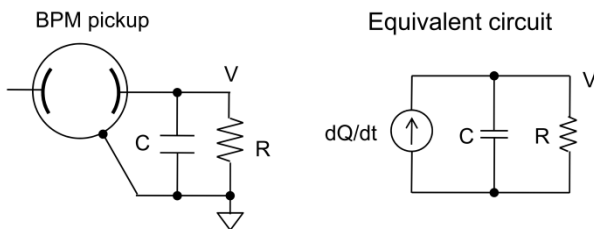

Figure 19: Equivalent circuit of a pickup.

In the observation of the beam bunch signal from the electrostatic pickup, we meet the problems due to the deformation of the signal wave-form by the signal transmission line resonance. As an example we consider the signal observation through a piece of coaxial cable as shown in Fig. 20. In usual case R_L is much larger than the characteristic impedance Z_0 of the cable because the condition of $R_L C >> \tau_b$ is required. Without the series resistor R between the electrode and the transmission cable, the wave-form of the signal voltage V is deformed by the reflection in the cable as shown in Fig. 21(a) and the frequency response has many resonant peaks as shown in Fig. 21(b).
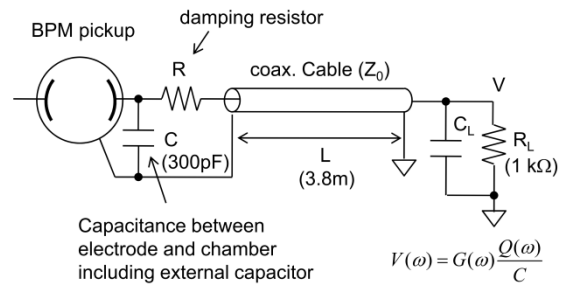

$$V(\omega) = G(\omega)\frac{Q(\omega)}{C}$$

Figure 20: Observation of pickup signal.
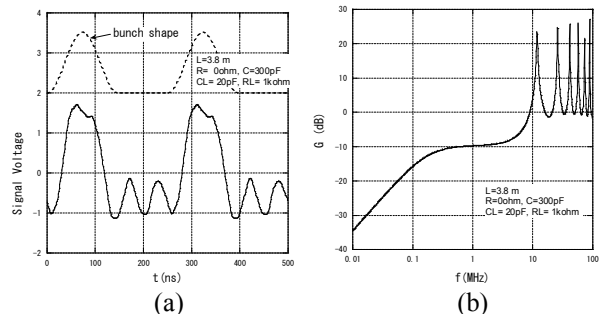

(a)   (b)

Figure 21: (a) observed signal wave-form, (b) frequency response. The dashed line shows the beam bunch shape.

The series resistor R shown in Fig. 20 is effective to damp these resonances as shown in Fig. 22 where $R=100$ Ω is assumed. These resonances are caused by the resonance of the capacitance C and the reactance component of the mismatched cable so that it is required to adjust R to minimize the resonance.
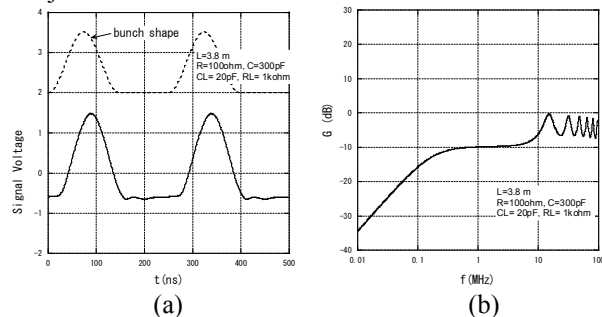

(a)   (b)

Figure 22: Resonance damping by the series resistor R.

Front End Electronics

Figure 23 is the diagram of the front end electronics of PEP-II BPMs [5]. The pickup electrode signal is filtered by band pass filter (BPF) to eliminate unnecessary frequency components except for the bunch spectrum. The filtered signals are demodulated by the I/Q demodulator to detect the amplitude of the beam spectrum. Demodulated signals are then filtered by the low pass filter (LPF) with 20 MHz bandwidth to determine the observation bandwidth. The "sin" and "cos" components from the I/Q demodulator are digitized by A/D converters to calculate the signal amplitudes and Δ/Σ of 4 button

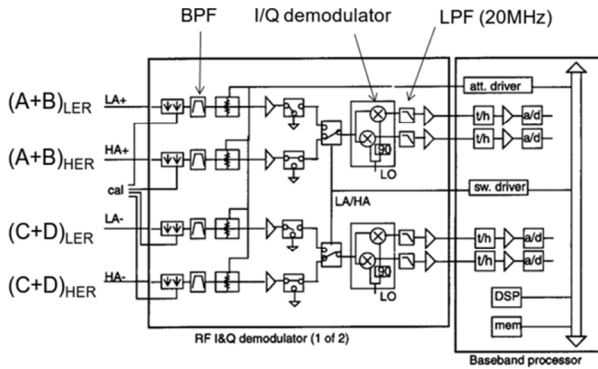signals. In the wideband mode, for example 20MHz bandwidth, the turn-by-turn beam position can be measured.

Figure 23: Block diagram of front end circuit of PEP-II BPMs.

KEKB BPM Signal Processing

To avoid technical difficulties related to the high precision I/Q demodulators, the KEKB BPM system of eliminated the analog demodulator circuit as shown in Fig.24 [4]. The signal from the pickup electrode is converted to the 99 kHz IF signal (intermediate frequency signal) by a super-heterodyne circuit. The IF signal is directly digitized and then processed in a DSP chip to detect the spectrum amplitude of the beam signal and calculate the Δ/Σ ratio of button signals. Four button signals from a BPM pickup are switched one-by-one and processed by one front end circuit, therefore, the system is specialized to the narrowband measurement of the closed orbit.
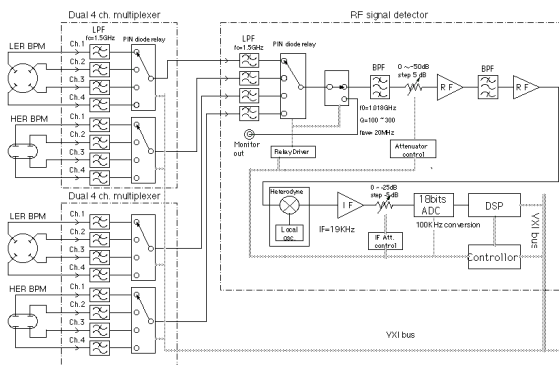

Figure 24: Front end circuit of KEKB BPMs.

J-Parc BPM Signal Processing

The front end electronics of the J-Parc BPM system is shown in Fig. 25 [6]. Because of the low rf frequency for beam acceleration (1.67-2.72 MHz), the signals from 4 pickup electrodes are filtered by LPF with cut-off frequency of 10 MHz and then digitized directly in parallel to calculate the Δ/Σ of the 4 electrode signals. The system is designed to measure the beam position in closed orbit measurement mode and also the single-pass

measurement mode. For the operation in single-pass mode, the ADCs with 80 MHz conversion frequency are employed.
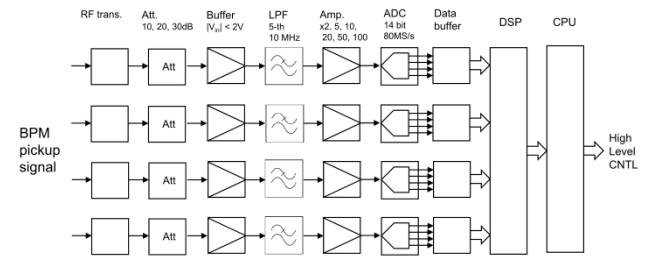

Figure 25: Front end circuit of the J-Parc BPM.

Log-ratio BPM

As mentioned in the previous section, the response of the log-ratio log(A/B) against the beam position displacement is more linear than that of the Δ/Σ of 2 signals from the pickup electrode A and B of the parallel electrode BPM (see Fig. 2). The log-ratio processing is realized by using two logarithmic amplifiers as shown in Fig. 26 [7] where the output is given by

$$V = K \log \frac{A}{B} = 2K \tanh^{-1} \frac{A-B}{A+B}.$$

Although the rf log-amplifier has wide dynamic range, there is small gain ripple against the input signal level. In the example shown in Fig. 27, the periodic error of the order of 1 % in the output due to the gain ripple is observed.
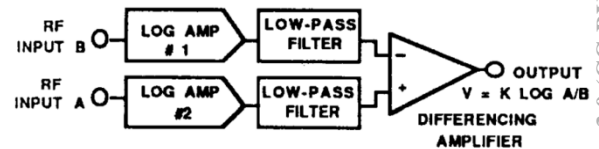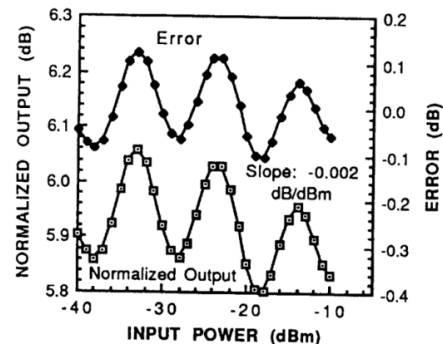

Figure 26: Log-ratio BPM circuit.

Figure 27: Error and normalized output of the log-ratio BPM.

For the 4-button BPM, the log-ratios of 4 signals A, B, C and D are defined by

$$X = \log(A/C) - \log(B/D), \quad Y = \log(A/C) + \log(B/D).$$

Figures 28 and 29 show an example of log-ratio BPM applied to the KEKB BPM and the measured mapping of X and Y. Comparing the mapping of Δ/Σ shown in Fig. 18, we can see that the log-ratio is more linear than the Δ/Σ.
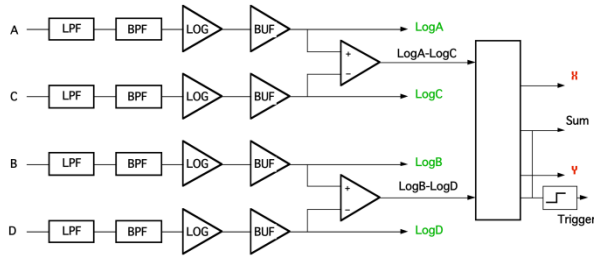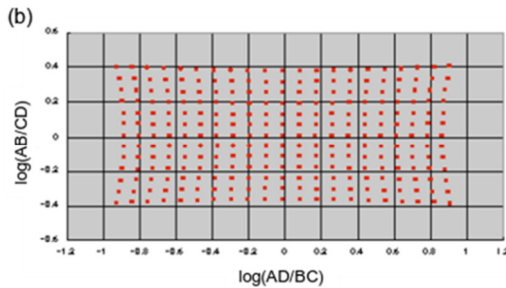

Figure 28: Log-ratio BPM applied to the 4 button BPM.

Figure 29: Mapping of log-ratio X and Y.

AM/PM Conversion Processing

In the amplitude-modulation-to-phase-modulation (AM/PM) method, the two rf signals from two pickup electrodes are converted to two equal amplitude signals whose phase difference is related to the amplitude ratio of two incoming signals. Figure 30 shows a diagram of the basic conversion process. The phases of equal amplitude re-combined signals at S_1 and S_2 indicated in the figure are given by

$$\theta_1 = -\theta_2 = \tan^{-1}(A/B),$$

where A and B are the amplitudes of incoming signals, and the resultant analog output of the phase detector becomes to be

$$V_{out} = V_0(\theta_1 - \theta_2 - \pi/2) = 2V_0 \tan^{-1}(\frac{A-B}{A+B}).$$

It is well known that the AM/PM processing method is employed at Fermilab Booster, Main Ring and Tevatron [8] because of the obtainable large dynamic range and high real-time bandwidth.
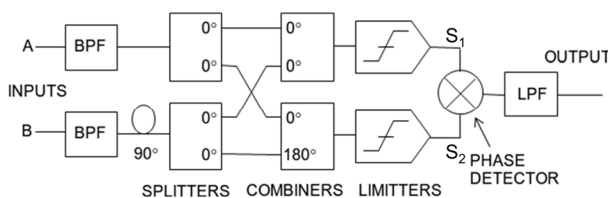

Figure 30: Block diagram of the basic AM/PM processing.

BEAM-BASED CHARACTERIZATION OF BPMS

The BPM system has many error sources: fabrication error of the pickups, contact errors of connectors, errors of cable impedance, setting errors of pickups, errors of signal processors, etc. The improvement of the overall performance of the BPM system can be accomplished by the beam-based calibration.

Beam Based Alignment

Beam based alignment (BBA) is the offset correction of BPM pickup based on the beam measurement. Each BPM pickup is installed in the accelerator to adjust the pickup center to the magnetic center of the adjacent quadrupole magnet. The BPM offset is calibrated by finding the position of the closed orbit at that BPM which is insensitive to a change of the field strength of the adjacent quadrupole magnet [9]. The orbit change by the field gradient change Δk of the quadrupole magnet is proportional to the closed orbit displacement Δx from the magnetic center of the quadrupole magnet. Measuring the orbit change for various Δx, the beam position insensitive to Δk can be found by fitting the data. The change of the closed orbit by Δk can be measured by any BPM in the ring. Fig. 31 shows an example of the offset position of a certain BPM observed by all BPMs in the ring at KEKB-HER.
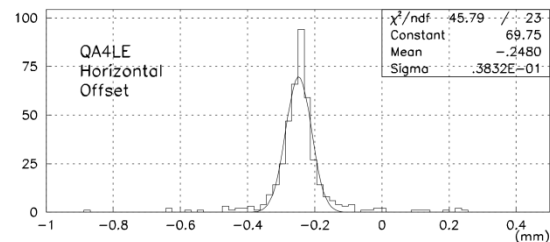

Figure 31: The beam position which is insensitive to a Δk of the adjacent quadrupole magnet. The beam position change is monitored by every BPM in the ring.

Figures 32(a)-(d) show the offset distributions for the HER and LER BPMs of the KEKB. Offsets of all BPMs in the KEKB ring were corrected by the measured offset data installed in the database. The effects of the BPM offset correction can be seen in the beam orbit. Figures 33 (a) and (b) show the COD with and without the offset correction for the LER. The orbit is smoother, especially in the arc sections, after the offset correction is included.
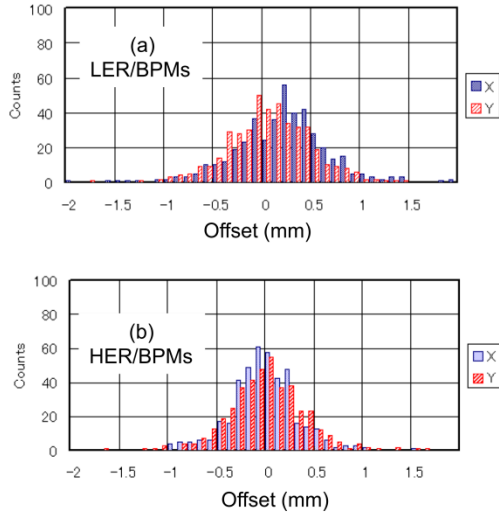
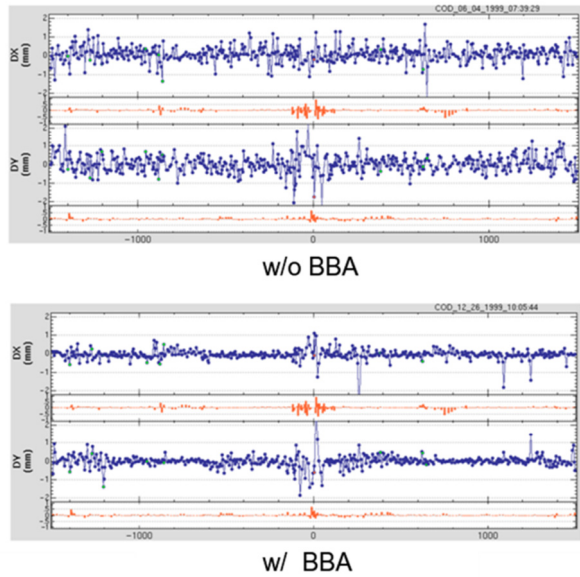Figure 32: BPM offsets. Blue bars and red bars show horizontal offsets and vertical offsets, respectively.

w/o BBA

w/ BBA

Figure 33: COD change by beam based alignment.

Beam Based Gain Calibration of 4 Button Pickups

The output signal of the i-th pickup electrode for the beam position (x, y) against the BPM pickup center is expressed as

$$V_i = qg_iF_i(x,y)$$

where g_i is the relative gain factor, $F_i(x,y)$ is the response function normalized to $F_i(0,0)=1$, and q is the proportional factor to the beam current. We consider m times measurements with different beam positions (x_j, y_j). For the 4-button BPM pickup ($i=1,\ldots, 4$) as illustrated in Fig. 34, we can determine 3m+3 unknowns of $g_2/g_1, \ldots, g_4/g_1, q_1,\ldots, q_m, (x_1,y_1),\ldots, (x_m,y_m)$ for m≥4 by the least squares method applied to

$$J = \sum_{i=1}^{4}\sum_{j=1}^{m}\{V_{i,j} - q_jg_iF_i(x_j,y_j)\}^2 ,$$

where $V_{i,j}$ is the measured signal voltage of i-the button electrode at j-th measurement. The response function of each button pickup electrode of 4 button BPM pickup can be expressed as [10]

$$
\left.
\begin{aligned}
F_1(x,y) &= 1 + a_1x + b_1y \\
&\quad + a_2(x^2 - y^2) + b_2(2xy) \\
&\quad + a_3(x^3 - 3x^2y) + b_3(3xy^2 - y^3) \\
&\quad + a_4(x^4 - 6x^2y^2 + y^4) + b_4(x^3y - xy^3) \\
&\quad + \cdots\cdots \\
F_2(x,y) &= F_1(-x,y), \quad F_3(x,y) = F_1(-x,-y) \\
F_4(x,y) &= F_1(x,-y)
\end{aligned}
\right\},
$$

The expansion coefficients a_k and b_k are determined by fitting the measured mapping at the calibration stand or the calculated mapping by the finite boundary element method. Figure 36 shows the example of the relative gain of the pickup electrode g_2/g_1, g_3/g_1 and g_4/g_1 of all BPM pickups in the ring obtained by beam based gain calibration at KEKB HER [11]. The residual errors of the least squares with a_k and b_k obtained from the calculated mapping data are smaller than those with a_k and b_k obtained from the mapping measurement at the calibration stand. Figure 35 shows the offset distribution of the LER and HER BPMs. Comparing Fig. 35 with Fig. 32, it can be seen that the offset distributions are improved by the beam based gain calibrations.
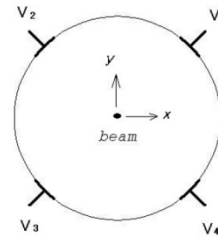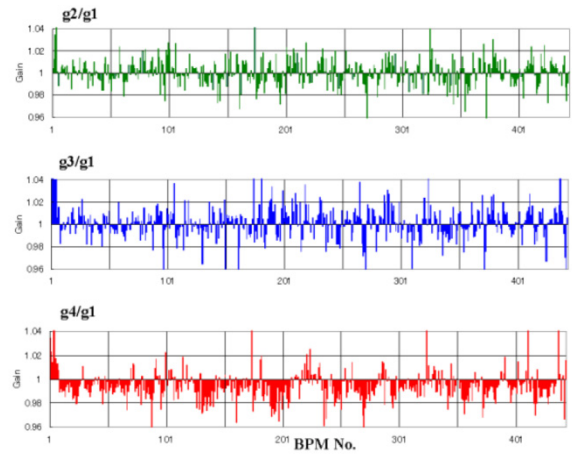

Figure 34: The 4-button BPM pickup.

Figure 35: Relative gains of button electrodes obtained by beam based calibration.
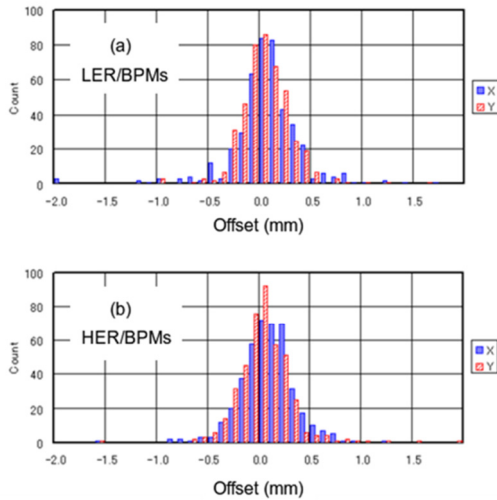
Figure 36: Offset distributions after the beam based gain calibration.

Beam Based Gain Calibration at J-Parc MR

The BPM pickups of the J-Parc MR consist of the electrostatic pickup electrodes of diagonal cut cylinder type as illustrated in Fig. 13 where the horizontal and vertical beam positions are independently detected by two pairs of pickup electrodes. For these linear response pickups, above mentioned least squares (LS) method minimizing the sum of the square of the difference between each electrode output and the model function is not applicable.

The outputs of diagonal cut electrodes for the beam position (x, y) are given by

$$V_L = \lambda(1 + x/a), \quad V_R = g_R\lambda(1 - x/a) \atop V_U = g_U\lambda(1 + y/a), \quad V_D = g_D\lambda(1 - y/a) \Big\}, \quad (7)$$

where λ is the proper normalization factor proportional to the beam current, g_R, g_U and g_D are the relative gain to the electrode L and g_L is normalized to 1, and a is the radius of diagonal cut electrode. From Eq. (7) we obtain the equation of

$$V_L = -\frac{1}{g_R}V_R + \frac{1}{g_U}V_U \frac{1}{g_D}V_D .$$

When beam positions are measured m times, we can expect the relation of

$$Ax = b, \quad (8)$$

where

$$A = \begin{pmatrix} -V_{R,1} & V_{U,1} & V_{D,1} \\ & \vdots & \\ -V_{R,j} & V_{U,j} & V_{D,j} \\ & \vdots & \\ -V_{R,m} & V_{U,m} & V_{D,m} \end{pmatrix},$$

$$x = \begin{pmatrix} 1/g_L \\ \vdots \\ 1/g_U \\ \vdots \\ 1/g_D \end{pmatrix}, \qquad b = \begin{pmatrix} V_{L,1} \\ \vdots \\ V_{L,j} \\ \vdots \\ V_{L,m} \end{pmatrix},$$

and $V_{i,j}$ denotes the measured output at j-th measurement of the electrode i ($i=R, L, U$ or D). The approximated solution of least squares (LS) of the linear system $Ax = b$ is given by

$$x_{LS} = (A^T A)^{-1} A^T b,$$

when the components of matrix A have no errors. On the other hand, when A has errors, the best approximated solution is given by total least squares (TLS) method [12]. The solution of TLS is given by

$$x_{TLS} = (A^T A - \sigma_{n+1}^2 I)^{-1} A^T b$$

where n is the rank of A and σ_{n+1} is the smallest singular value of the matrix $[A \ b]$. The simulation with the TLS method for Eq. (8) indicates good reproducibility of gain errors. Examples of relative gains of electrodes of two BPMs (BPM001 and BPM002) at the J-Parc MR obtained by LS and TLS methods are listed in Table 1 and corrected beam positions using corrected pickup gains by TLS method are shown in Fig. 37 for two BPMs [11].

Table 1: Corrected relative gains of pickup electrodes by TLS and LS methods.

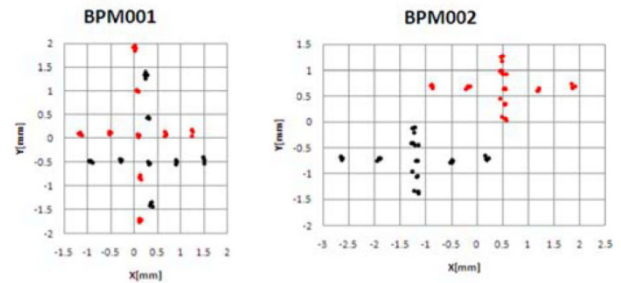| BPM001	g_2	g_3	g_4
TLS	1.0062	1.0024	0.9873
LS	1.0103	1.0045	0.9892
BPM002	g_2	g_3	g_4
TLS	0.9568	0.9811	0.9463
LS	0.9617	0.9838	0.9487

Figure 37: Measured beam position at two BPMs. Red points are the measured positions without gain correction. Black points are the corrected positions with TLS method.

Resolution Measurement with 3-BPM Correlation Method

The beam positions at neighboring three BPMs as shown in Fig. 38 are linearly related by

$$x_3 = Ax_1 + Bx_2 + C , \qquad (9)$$

if there is no nonlinear element between BPMs. The coefficients A, B and C are determined by fitting Eq. (9) as shown in Fig. 39 with the least squares method minimizing

$$J = \sum_j \{x_{3,j} - (Ax_{1,j} + Bx_{2,j} + C)\}^2 ,$$

where $x_{i,j}$ is the measured value of x_i at the j-th measurement. Assuming same resolution of three BPMs, the BPM resolution σ is given by

$$\sigma = \sqrt{\frac{1}{N-1} \frac{\sum_j^N \{x_{3,j} - (Ax_{1,j} + Bx_{2,j} + C)\}^2}{1 + A^2 + B^2}} .$$

Figure 40 shows an example of the measured vertical BPM resolution at the J-Parc MR [13].
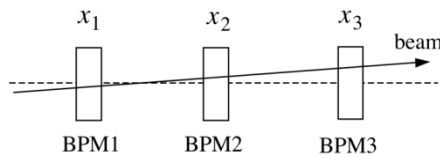

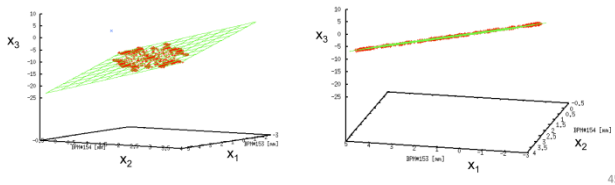Figure 38: Beam positions at neighboring three BPMs.

Figure 39: Distribution of beam positions (x_1, x_2, x_3) measured by 3 BPMs. Green lines represent the plane fitted to the measured points with least squares.
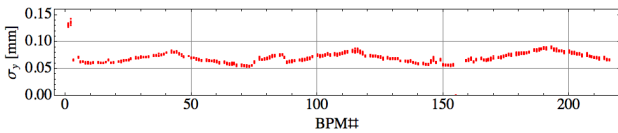

Figure 40: Measured BPM resolutions at J-Parc MR.

Figure 41 shows BPM resolutions of the KEKB HER (electron storage ring) measured by 3 BPM correlation method [4]. The average resolution is 1.9 μm which is better than that of the J-Parc proton synchrotron.

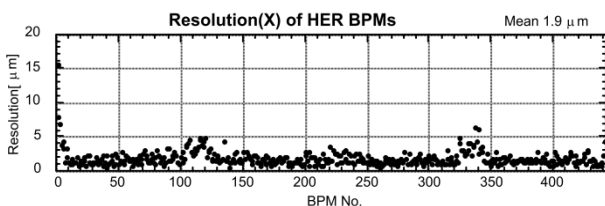Figure 41: Measured BPM resolutions at KEKB LER.

COUPLING IMPEDANCE OF BPM PICKUPS

Emittance Blow-up by BPM Pickup Impedance at KEK PS

We have a possibility of beam instability caused by coupling impedances of BPM pickups because large number of BPM pickup will be installed in the accelerator. At the KEK proton synchrotron (PS) the beam blow-up caused by the resonant impedances of the BPM pickups was one of the causes of the beam loss at the phase transition [14]. Before 1996 the KEK PS employed wall current-pickup type BPMs and the resonances associated by the cavity structure between the current pickup electrode of the BPM and the BPM chamber were confirmed by the impedance measurement at the coaxial line test bench as shown in Fig. 42(a) and the MAFIA calculation. In 1997 the wall current-pickup type BPMs were replaced by electrostatic type BPMs illustrated in Fig. 43 and no resonance up to 1.8 GHz was confirmed for the replaced BPMs as shown in Fig. 42(b). By replacing BPM pickups the longitudinal emittance blow-up was improved as shown in Fig. 44.

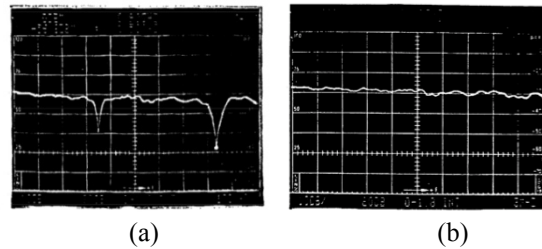(a)   (b)

Figure 42: Transmission parameter s_{21} measured by stretched-wire current method. (a) Wall current pickup type BPM. (b) Electrostatic type BPM.
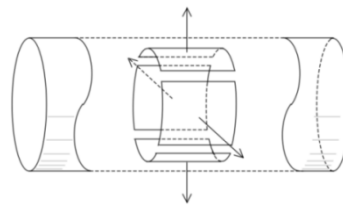

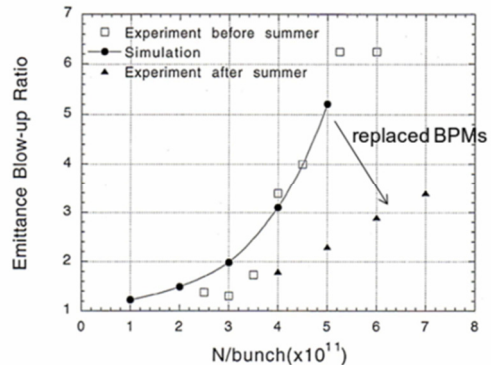Figure 43: Electrostatic type BPM pickup with parallel 4 electrodes.

Figure 44: Improvement of longitudinal emittance blow-up by the replacement of BPMs.

Coupling Impedance of PEP-II BPMs

The detail analysis of the BPM coupling impedance based on the 3D electromagnetic field calculation by the MAFIA code was performed for the PEP-II BPMs shown in Fig. 45 [15]. The calculated spectrum of the longitudinal impedance of a 4 button BPM pickup of PEP-II is shown in Fig. 46 [14]. A sharp peak of 25 Ω is seen at around 6.8GHz. The total impedance of all BPMs in a ring due to this resonant mode is 6.5 kΩ. Although the acceptable impedance will be 3.4 kΩ to avoid multi-bunch instabilities at the design beam current of 3A if only the radiation damping is taken into account for the damping mechanism, this impedance was accepted by expecting other damping mechanisms such as beam feedback. As for the broadband impedance calculated impedance of $|Z_{//}/n|$=0.008 Ω is much smaller than the maximum acceptable ring impedance of 0.5 Ω to avoid single-bunch instabilities.
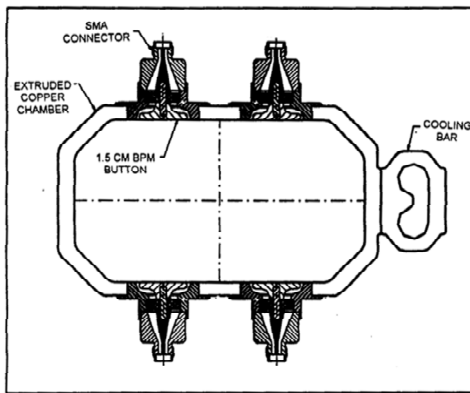

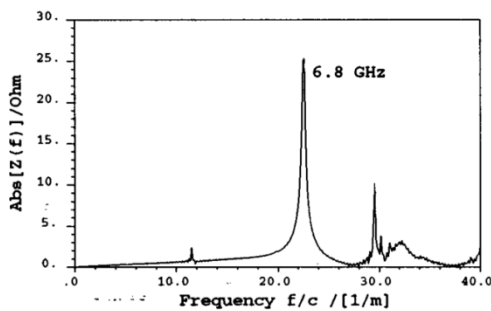
Figure 45: Layout of the 4 buttons of a PEP-II BPM.

Figure 46: Longitudinal impedance spectrum of a PEP-II BPM.

Coupling Impedance of KEKB BPMs

The coupling impedance calculations of BPMs similar to the PEP-II BPMs were also performed for the KEKB BPMs shown in Fig. 15 [16]. The calculation shows that the longitudinal impedance spectrum has sharp peak at around 7.6 GHz. The calculation results by MAFIA code are listed in Table 3. The total shunt impedances of all BPMs are 3.6 kΩ for the LER and 7.7 kΩ for the HER. Although the asymmetric structure of the button electrode was employed for the HER BPMs, no meaningful

suppression of the impedance was observed. The acceptable beam current to avoid the longitudinal multi-bunch instabilities is strongly dependent on the bunch fill pattern in the ring. In the every 4 bucket bunch filling operation of each ring, the acceptable beam currents are expected to be 1.6A for the LER and 2.6A for the HER. To decrease the coupling impedance the small button electrode with half diameter of the KEKB BPM button is planned for the next SuperKEKB.

Table 2: Longitudinal Impedance of KEKB BPMs

	f_R (GHz)	R_s (Ω)	NR_s (kΩ)	Q	I_{max} (A)
LER	7.61	8.1	3.6	137	1.6
HER	7.57	17.4	7.7	91	2.4

Broad-band impedance $|Z_{//}/n|$: 0.0014 Ω (LER)
                                                      0.004 Ω (HER)

DISPLACEMENT PROBLEM OF BPM PICKUPS

Even though BPM pickups are fixed to the adjacent quadrupole magnets rigidly to keep the relative position of BPM to the adjacent magnet, unpredictable displacement of the BPM pickup happens sometimes at high current electron or positron rings such as KEKB. At KEKB the displacements of BPM pickups depending on the beam current were observed as shown in Fig. 47 [17]. The BPM pickups were displaced by the large thermal deformations of the beam chambers exceeding the tolerances of the bellows connecting beam chambers and BPM pickups caused by the irradiation of the strong synchrotron radiation. The closed orbit was corrected at every 10-20 sec based on the COD measurement with BPMs. Therefore the change of betatron tune was caused by the change of the beam position at the sextupole magnets as shown in Fig. 48. To overcome the displacement problem of BPMs , the displacements of BPM pickups were measured by displacement sensors to correct the BPM offsets in real time.
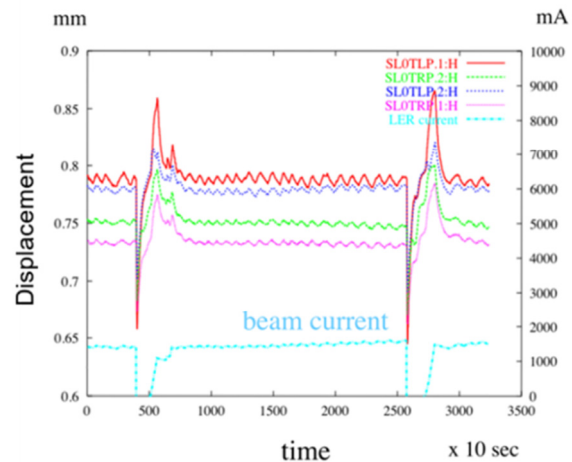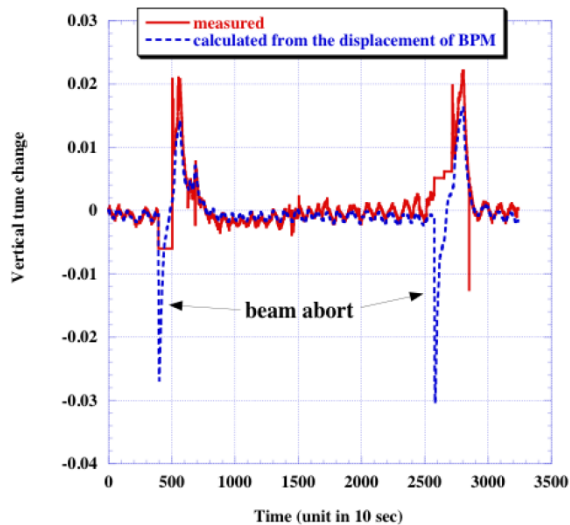

Figure 47: Displacements of BPM pickups at KEKB.

Figure 48: Vertical tune change by the displacements of BPM pickups.

CONCLUDING REMARKS

We have many issues to be considered for design and construction of the BPM system as mentioned in the text. It is one of the difficult problems to guarantee the precise measurement of beam positions for different operations of accelerators. For example the operation condition of accelerators at the commissioning stage or the machine study is very different from the routine operation. To guarantee the accuracy of the beam position measurement at various operation conditions, it is important to fully understand the beam diagnostic devices and also the accelerator facility.

REFERENCES

[1] R. E. Shafer, AIP Conf. Proc. 249 (1992) 601.
[2] T. Shintake et al. NIM A254(1987)146.
[3] T. Toyama et al. Proceedings of DIPAC2005, Lyon, France, p. 270.
[4] M. Arinaga et al. Nucl. Instrum. Meth. , A499(2003) 100.
[5] G. Roberto et al. Proc. 7th Workshop on Beam Instrumentation, 1996, AIP Conf. Proc. 390, p.341.
[6] T. Toyama, private communication.
[7] F. D. Wells et al. Proc. 1991 Particle Accelerator Conf. p.1139.
[8] R. E. Shafer et al. IEEE Trans. Nucl. Sci. 28, 1981, p.2323.
[9] M. Masuzawa et al. Proceedings of EPAC 2000, Vienna, Austria, p.1780.
[10] K. Satoh and M. Tejima, Proceedings of the 1997 Particle Accelerator Conference, Vancouver, Canada, p. 2087.
[11] M. Tejima et al. Proceedings of DIPAC2011, Humburg, Germany, p. 275.
[12] I. Markovsky and S. V. Huffel, Signal Processing 87 (2007) 2283.
[13] T. Toyama et al. Proceedings of IPAC'10, Kyoto, Japan, p. 981.
[14] K. Takayama et al. Phys. Rev. Lett. 3 (1997) 871.
[15] C. –K. Ng et al. SLAC-PUB-95-6899, May 1995.
[16] K. Shibata et al. Proc. 2007 Particle Accelerator Conf. 2007, p. 4048.
[17] M. Tejima et al. Proceedings of 2005 Particle Accelerator Conference, Knoxville, Tennessee, p. 3253.